Dalton
Transactions

Atomic Layer Deposition of Lithium Zirconium Oxides for Improved Performance of Lithium-ion Batteries

Journal:	*Dalton Transactions*
Manuscript ID	DT-ART-10-2021-003600.R2
Article Type:	Paper
Date Submitted by the Author:	07-Jan-2022
Complete List of Authors:	Liu, Yongqiang; University of Arkansas Fayetteville, Mechanical Engineering Wang, Xin; University of Arkansas Fayetteville, Mechanical Engineering Ghosh, Sujan Kumar; University of Arkansas Fayetteville, Mechanical Engineering Zou, Min; University of Arkansas Fayetteville, Mechanical Engineering Zhou, Hua; Argonne National Lab, Advanced Photon Source Xiao, Xianghui; Brookhaven National Laboratory Meng, Xiangbo; University of Arkansas Fayetteville, Mechanical Engineering

Atomic Layer Deposition of Lithium Zirconium Oxides for Improved Performance of Lithium-ion Batteries

Yongqiang Liu[1,3], Xin Wang[1], Sujan Kumar Ghosh[1,2], Min Zou[1,2], Hua Zhou[4], Xianghui Xiao[5*], and Xiangbo Meng[1,2*]

[1]Department of Mechanical Engineering, The University of Arkansas, Fayetteville, AR 72701, USA

[2]The Center for Advanced Surface Engineering, The University of Arkansas, Fayetteville, AR 72701, USA

[3]College of Science, Northeast Forestry University, Harbin 150040, Heilongjiang, China

[4]Advanced Photon Source, Argonne National Laboratory, Lemont, IL 60439, USA

[5]National Synchrotron Light Source II, Brookhaven National Laboratory, Upton, NY 11973, USA

* Corresponding author: xbmeng@uark.edu; xiao@bnl.gov

ABSTRACT: Recently there has been an increasing interest to develop lithium-containing films as solid-state electrolytes or surface coatings for lithium-ion batteries (LIBs) and beyond systems. In this study, we for the first time investigated the thin film growth of lithium zirconium oxides (Li_xZr_yO or LZOs) through combining two individual atomic layer deposition (ALD) processes of ZrO_2 and LiOH, i.e., sub-ALD of ZrO_2 and LiOH. We revealed that the hygroscopic nature of the LiOH component has a big impact on the growth of LZOs. We found that an increased temperature to 225 ℃ was more effective than an elongated purge to mitigate the adverse effects of the physisorbed H_2O. We further discovered that, during the resultant LZO super-ALD processes, the growth of the sub-ALD LiOH has been promoted while the growth of sub-ALD ZrO_2 has been inhibited. In this study, a suite of instruments has been applied to characterize the LZO super-ALD processes and the resultant LZO films, including *in-situ* quartz crystal microbalance (QCM), scanning electron microscopy (SEM), transmission electron microscopy (TEM), atomic force microscopy (AFM), synchrotron-based X-ray diffraction (XRD), and X-ray photoelectron spectroscopy (XPS). Furthermore, we applied the resulting LZO films over $LiNi_{0.6}Mn_{0.2}Co_{0.2}O_2$ (NMC622) cathodes in LIBs and demonstrated that the LZO coating films could evidently improve the lithium-ion insertion and extraction rates of NMC622 electrodes up to 3.4 and 2.6 times, respectively. The LZO-coated NMC622 cathodes exhibited much better performance than that of uncoated NMC622 ones.

1. Introduction

In lithium-ion batteries (LIBs), interfaces take some critical roles related to battery safety, cyclability, and Columbic efficiency.[1-2] They are located at between either of the anode and cathode and the electrolyte, where undesirable reactions occur and consume lithium (Li) and the electrolyte with the formation of solid electrolyte interphases (SEIs).[3] In general, SEIs are unstable and their continuous decomposition and formation are prone to deplete the electrolyte and result in cell failure. To this end, many different strategies have been developed to surface-modify electrodes and thereby improve their stability and properties.[4-7] In the past decade, atomic layer deposition (ALD) has emerged as a new surface-modification technique, featuring its unrivaled capabilities enabling uniform and conformal coatings at moderate temperatures with the growth preciseness at the atomic level.[8-11] Particularly, it is to date the only technique that can deposit coatings directly on prefabricated electrodes. These coatings have beneficial effects in multiple aspects, such as (i) serving as a physical barrier between the electrode and electrolyte, which mitigates irreversible side reactions, (ii) protecting the electrode from corrosive attacks, and (iii) enhancing the mechanical integrity of the electrode.[8, 12] Since the first Li-containing coating (i.e., $LiAlO_2$) by ALD was practiced to protect LIBs in 2014,[13-14] there have been many more such coatings investigated, as recently reviewed by Meng.[15] In the review, Meng made a systematic summary on all lithium-containing films by ALD and discussed their fabrication processes. Compared to binary oxides (e.g., Al_2O_3, TiO_2, and ZrO_2),[12, 16-17] Li-containing coatings generally exhibit better ionic conductivity that facilitates the transport of Li-ions through the interfaces. Thus, there has been an increasing interest in developing Li-containing films as surface coatings of LIBs.

In pursuing next-generation LIBs, the nickel (Ni)-rich $LiNi_{0.6}Mn_{0.2}Co_{0.2}O_2$ (NMC622) oxide is among the most promising cathodes, ascribed to its high capacity and low cost.[18-19] However, NMC622 suffers from a series of interconnected issues, such as micro-cracking, metal dissolution, irreversible phase transition, and so on.[20-21] In fact, all these issues are interface-related. Thus, it's extremely critical to establish a stable interface for achieving high-performance NMC622. To this end, various ALD coatings have been investigated and have shown some beneficial effects enabling better performance of LIB cathodes. Among them, several Li-containing coatings were reported for better performance of LIB cathodes than binary oxides did, such as

$LiAlO_2$,[13-14] $LiTaO_3$,[22] $LiAlF_4$,[23] Li_3PO_4,[24] and LiPON.[25-26] To fabricate such ternary or quaternary lithium-containing compounds via ALD, one strategy was to integrate two or more sub-ALD systems into a super-ALD process, in which a sub-ALD LiOH was generally involved as the Li source. The most widely used LiOH process adopted the lithium tert-butoxide (LiO^tBu or LTB) and water as its precursors, first studied by Cavanagh et al.[27] They also revealed that this resultant LiOH film is highly hygroscopic. In a later work, Comstock and Elam further disclosed that the hygroscopic nature of this LiOH ALD was very troublesome to produce Li-rich Li_xAl_yO by tuning the sub-cycle ratio of the two sub-ALD processes: LiOH and Al_2O_3.[28] They found that, with a sub-cycle ratio of LiOH/Al_2O_3 higher than 1:1, multiple sub-ALD cycles of LiOH in a series were prone to accumulate more physisorbed water and thereby to cause non-self-limiting growth of the subsequent Al_2O_3.[28] However, a sub-cycle ratio lower than or equal to 1:1 was always able to grow Li_xAl_yO linearly. As a consequence, the Li_xAl_yO super-ALD was limited to grow films with the cation ratio of Li/(Li+Al) less than 55%. Among Li_xM_yO (M = metal) ALD processes reported to date, a linear growth was typically reported for one sub-cycle of LiOH integrated with one or multiple MO_x sub-cycles, such as Li_xTa_yO [29] and Li_xNb_yO.[30]

Stimulated by the benefits of Li-containing coatings, in this study we attempted to develop a class of new Li-containing oxides, lithium zirconium oxides (LZOs) through combining and tuning two individual sub-ALD processes, LiOH and ZrO_2 with different sub-ALD cycle ratios, m/n, where m and n are the sub-ALD cycles of LiOH and ZrO_2, respectively. The LiOH and ZrO_2 sub-ALD processes have been reported previously.[31-34] In this study, we focused on clarifying the growth characteristics of ALD LZOs at different ALD parameters and their effects on the performance of NMC622 electrodes. We found that the growth of the proposed LZO super-ALD processes were subject to the hygroscopic nature of the LiOH sub-ALD. To mitigate the hygroscopic effects of the LiOH sub-ALD, we revealed that a relatively high ALD temperature, e.g., 225 ^oC, was essential for establishing a stable super-ALD process for LZOs. We also demonstrated that the resultant LZO coatings could remarkably improve the cyclability of NMC622 electrodes, due to their better Li-ion insertion and extraction rates than that of SEIs.

2. Experimental

2.1. ALD-LZOs

The ALD experiments utilized a commercial ALD reactor (Savannah 200, Cambridge Nanotech Inc., Cambridge, MA).[16-17, 31] LZO films were prepared by combining two individual sub-ALD processes of LiOH and ZrO_2. The LiOH sub-cycle consisted of two alternative doses, LTB (98%, Strem Chemicals, Inc., USA) and deionized H_2O. The ZrO_2 ALD was performed with two alternative doses, tetrakis(dimethylamido)zirconium (IV) (TDMA-Zr) and deionized H_2O. The solid LTB precursor was heated to 150 ℃ while TDMA-Zr was heated to 75 ℃ to provide sufficient vapor pressure. The ALD deposition temperatures of LZOs were 175, 200, or 225 °C. Either of the two sub-ALD processes was operated with a time sequence, $t_1-t_2-t_3-t_4$, where t_1 and t_3 were the precursor dosing times for LTB (or TMDA-Zr) and water, respectively, and t_2 and t_4 were the Ar purging times after the doses, respectively. The optimal dosing time of the LTB was studied between 1 and 6 *s*. In this study, three different sub-cycle ratios (*m/n*) between sub-ALDs of LiOH and ZrO_2 were investigated, i.e., 1:2, 1:1, and 2:1 ALD-LZO. Particularly, the ALD system was integrated with a glove box and this integrated system ensured no air exposure to the ALD-deposited films.

2.2 Materials characterization

In-situ quartz crystal microbalance (QCM) measurements were conducted using a quartz crystal (Inficon, USA). To constitute a repeatable surface, a 50-cycle ALD-Al_2O_3 film (using trimethylaluminum (TMA) and H_2O as precursors) was performed prior to each deposition of ALD-LZOs, as practiced in our previous studies.[35-37] The LZO films were deposited on nitrogen-doped graphene nanosheets (N-GNS) and observed using a scanning electron microscopy (SEM, XL30, Philips FEI, Hillsboro, OR). Topographical analyses of LZO thin films were performed using an atomic force microscope (AFM, Dimension Icon, Bruker Nano Surfaces, Billerica, MA). Synchrotron-based X-ray diffraction (XRD) was used to determine the crystallinity of the LZO films and performed at the beamline 12-ID-D at Advanced Photon Source (APS) at Argonne National Laboratory (ANL, IL, USA). The X-ray wavelength was 0.6199 Å. TEM specimens were prepared from LZO-coated NMC622 electrodes using a focused ion beam (FIB) (Zeiss NVision 40) through standard lift-out process. The elemental distribution was mapped using a scanning transmission electron microscopy (STEM, FEI Talos F200X) equipped with a SuperX EDS detector. An X-ray photoelectron spectroscopy (XPS, Versa Probe III) was employed to investigate the elemental components of the ALD-LZOs. The morphological structure evolution in NMC particles at mesoscale resolution (30 nm) was characterized with synchrotron-based transmission X-ray microscopy (TXM) at National Synchrotron Light Source II at Brookhaven National Laboratory.

2.3 Electrochemical evaluations

The NMC622 electrode slurry was prepared using a recipe of 86 wt.% NMC622 active material, 7 wt.% carbon black, and 7 wt.% poly-vinylidene fluoride binder (PVDF, MTI Corporation) with a certain amount of N-methyl pyrrolidinone using a mixer (AR-100, THINKY, USA). The obtained slurry was then casted onto Al foils and then expanded into laminates using a doctor blade. The laminates were first naturally dried in a canopy fume hood for one day and then further dried at 100 °C for 10 h under vacuum. The obtained electrodes were punched into 7/16″ disks with a mass loading of ~11.8 mg/cm^2. The NMC622 electrodes were coupled with lithium metal chips as anodes and assembled into CR-2032-type coin cells for electrochemical evaluations. The electrolyte was composed of 1.2 M $LiPF_6$ salt dissolved in ethylene carbonate (EC):ethyl methyl carbonate (EMC) with a 3:7 mass ratio. To analysis the lithium insertion/extraction behavior, cyclic voltammetry (CV) tests were performed on a versatile multichannel potentiostat (SP-200, BioLogic, USA) at various scan rates 0.1, 0.2, 0.3, 0.4, 0.5, 0.6, 0.7, 0.8, 0.9, and 1.0 mV/s) between 3.0 - 4.5 V (vs. Li/Li$^+$). Charge–discharge characteristics were tested using a battery tester (Neware, BTS2300, Shenzhen, China).

3. Results and Discussion

3.1 *In situ* QCM measurements of ALD LiOH and ZrO_2.

A sub-ALD LiOH (ALD-LiOH) process and a sub-ALD ZrO_2 (ALD-ZrO_2) process were tuned with different sub-ALD cycles (*m*/*n*) for different super-ALD LZO processes (super-ALD-LZOs). Prior to super-ALD LZOs, we have first attempted to determine the suitable heating temperature and dosing time of LTB. As shown in Figure S1a in Supporting Information, when LiOH is deposited at 225 °C, the mass gain per cycle (MPC) of LiOH increased with the increased heating temperatures of the LTB precursor, accounting for ~25 ng/cm^2 at 130 °C and ~32 ng/cm^2 at 140 °C or higher. Fixing the heating temperature of LTB at 150 ^{o}C, we studied the effects of dosing times of LTB on the growth of LiOH at 225 °C. As shown in Figure S1b, the ALD-LiOH MPC gradually increased from ~17.3 ng/cm^2 at the dosing time of 1 *s* to ~30.5 ng/cm^2 at 3 *s*, and finally stabilized at a constant value about 31.8 ng/cm^2 at 6 *s*. To ensure the saturation growth of LiOH, we selected 150 °C and 3 *s* as the heating temperature and dosing time of LTB, respectively, in this work.

The ALD-LiOH process has been well studied previously.[34, 38] We confirmed that the growth of ALD-LiOH includes a nucleation regime (Region I) and a growth regime (Region II), as shown in Figure S2a. In the nucleation regime (Figure S2b), The MPC ($\Delta m_1 = \Delta m_{1A} + \Delta m_{1B}$) is ~25.6 ng/cm^2, in which the mass increase after a dosing of LTB (Δm_{1A}) is ~42.2 ng/cm^2, and the mass decrease after each exposure of H_2O (Δm_{1B}) is ~16.6 ng/cm^2. Thus, $|\Delta m_{1A}/\Delta m_{1B}|$ = ~2.54, which indicates that the deposited film might be $LiOH{\cdot}H_2O$, as discussed previously by Cavanagha et al.[27] The surface reactions could be described using Equation 1A and 1B as follows:

$$|\text{-LiOH} + \text{LiOC}(\text{CH}_3)\ (g) \rightarrow |\text{-LiOH-LiOC}(\text{CH}_3)_3 \qquad (1A)$$

$$|\text{-LiOH-LiOC}(\text{CH}_3)_3 + 2\text{H}_2\text{O}\ (g) \rightarrow |\text{-LiOH-LiOH}{\cdot}\text{H}_2\text{O} + \text{HOC}(\text{CH}_3)_3\ (g) \qquad (1B)$$

where "|" indicates the substate surface and "*g*" signifies the vapor phase. We also confirmed that, after the first 20 ALD cycles, the ALD-LiOH entered the so-called growth regime (Figure S2c). In this region, the mass first increased sharply and then decrease slowly during a following purge attributed to the hygroscopicity of $LiOH{\cdot}H_2O$.

Previously, we have studied ALD-ZrO_2.[31] In this study, we again measured the ALD ZrO_2 using the timing sequence of 0.03-*s* TDMA-Zr – 60-s purge – 0.015-s H_2O – 60-*s* purge at 225 °C. As shown in Figure S3b, the MPC of ALD-ZrO_2 ($\Delta m_2 = \Delta m_{2A} + \Delta m_{2B}$) is ~ 40 ng/cm^2. Assuming the crystalline ZrO_2 density of 6.16 g/cm^3, we estimated that the ALD-ZrO_2 has a growth per cycle (GPC) of 0.65 Å/cycle, equivalent to the one reported in our previous study using a purging time of 10 *s*.[31] According to our previous study,[31] the possible surface reactions of the ALD-ZrO_2 might be the ones as follows:

$$|\text{-(OH)}_3 + \text{Zr}(\text{NMe}_2)_4 \rightarrow |\text{-O}_3\text{-Zr}(\text{NMe}_2) + 3\text{HNMe}_2 \qquad (2A)$$

$$|\text{-}O_3\text{-}Zr(NMe_2) + 2H_2O \rightarrow |\text{-}O_2\text{-}Zr\text{-}(OH)_3 + HNMe_2 \qquad (2B)$$

3.2 *In situ* QCM measurements of ALD-LZOs.

Combining the two sub-ALD processes of LiOH and ZrO_2 in different sub-cycle ratios, we deposited LZO thin films at different temperatures: 175, 200, and 225 °C. Figure 1a shows the growth of 1:1 ALD-LZO at 175 °C, in which there are two regions identified, Region I and II. In Region I (the first 10 ALD cycles), there were distinct mass changes detected after the dosing of each precursor. As shown in Figure 1b, the MPCs of the sub-ALD LiOH and sub-ALD ZrO_2 are ~25.39 and ~58.3 ng/cm^2, respectively. In Region II, however, the mass changes due to the TDMA-Zr and H_2O doses were nearly unobservable (see Figure 1c). We suspected that the physisorbed water molecules during the sub-ALD of LiOH probably have "shielded" the susequent sub-ALD ZrO_2 from grwoth. Upon this phenomenon, we postulated that the TDMA-Zr precursor might have reacted with the top layer of the accumulated physisorbed water molecules but under the vacuum operational ALD system the resultant products could not stay on the deposited film due to the desorption of the physisorbed water in the underlayer. Such a phenomenon was like a "shielding" effect formed on TDMA-Zr by the physisorbed water. However, the accumulated physisorbed water would not affect the subsequent deposition of the sub-ALD of LiOH, due to its hygroscopic nature as confirmed in previous studies.[27-28] To verify our postulation, we thought that increasing deposition temperature or/and elongating purges would be effective to reduce physisorbed water and thereby to mitigate such a "shielding" effect. Thus, we increased the deposition temperature to 200 °C. Consequently, we observed two growth regions as well, as shown in Figure 1d. However, the Region I at 200 °C has been extended to 35 ALD cycles. Accordingly, the MPCs of the sub-ALD LiOH and the sub-ALD ZrO_2 in Regions I were ~15.65 and ~45.53 ng/cm^2 (Figure 1e), respectively. After the first 35 cycles, however, the super-ALD of LZO again entered a Region II, in which the growth of the sub-ALD ZrO_2 could not be detected again (Figure 1f). To this end, we further inceased the deposition temperature to 225 °C. Encouragingly, the 1:1 ALD-LZO could realize a linear growth with the distinct growth characteristics of both the sub-ALD LiOH and ZrO_2 for 50 ALD cycles (Figure 1g). Figure 1h clearly shows the MPC evolutions with the sub-ALD LiOH (Δm_1 ~ 15.35 ng/cm^2) and the sub-ALD ZrO_2 (Δm_2 ~ 32.19 ng/cm^2). Compared with the pure individual ALD-LiOH and ALD-ZrO_2 processes, the sub-ALD LiOH has a larger MCP (~15.35 vs. ~11.5 ng/cm^2 for a pure

LiOH ALD) while the sub-ALD ZrO_2 has a lower MCP (~32.19 vs. ~40 ng/cm^2 for a pure ZrO_2 ALD). This suggests that the growth of the sub-ALD LiOH was promoted by the sub-ALD ZrO_2 while the latter was inhibited in its growth by the former at 225 °C. Supposing the deposited LZO film was consisted of $LiOH{\cdot}H_2O$ by the sub-ALD LiOH and ZrO_2 by the sub-ALD ZrO_2, which has a molecular weight of M_1 (42 g/mol) and M_2 (123 g/mol), respectively. Based on the QCM data, thus, we estimated that the molar ratio between LiOH and ZrO_2 in the deposited LZO film is ~1.4, calculated by $(\Delta m_1/M_1)/(\Delta m_2/M_2)$. Consequently, the 1:1 ALD-LZO has probably resulted in a film of $Li_{1.4}ZrO_{3.4}$.

We also have studied the effects of purging times on the desorption of physisorbed H_2O during the 1:1 ALD-LZO. We found that the ALD-LZO could remain a stable growth for 10 consecutive cycles of Region I (see Figure 1a) but switched into a growth of Region II thereafter. We further revealed that, after every 10 consecutive cycles, a 20 min purging could ensure the growth of the ALD-LZO unchanged for two segments of 10 consecutive cycles, as shown in Figure S4a. After the third segment, there had no distinct growth of the sub-ALD ZrO_2 again, as shown in Figure S4b. This finding is significant, for it again confirms that the physisorbed H_2O molecules did form a "shielding" effect on the following growth of the sub-ALD ZrO_2. It is critical to eliminate such an effect to ensure a stable growth of ALD-LZO. In this regard, higher deposition temperatures and longer purges both are effective.

We further investigated 1:2 and 2:1 super-ALD processes of LZOs. Figure 2a shows that the 1:2 ALD-LZO could proceed linearly at 225 °C. Figure 2b clearly exhibits the distinct MPCs due to the sub-ALD processes of LiOH and ZrO_2. The sub-ALD LiOH has a repeatable MPC of ~14.58 ng/cm^2 and the MPCs of the sub-ALD ZrO_2 are ~32.67 and ~28.62 ng/cm^2 for the first and second sub-cycle, respectively. Based on these QCM data, we estimated that the molar ratio of LiOH and ZrO_2 is ~0.7, indicating a chemical formula of $Li_{0.7}ZrO_{2.7}$ for the 1:2 ALD-LZO. The 2:1 ALD-LZO super-ALD has also been studied, as shown in Figure S5. After ~7 super-ALD cycles, an evident "shielding" effect due to the physiosorbed H_2O was observed and led to an undetected growth of the sub-ALD ZrO_2. Apparently, a larger sub-cycle ratio than 1:1 led to the difficulty of a stable ALD-LZO. Given these facts, we mainly discuss the results of the stable 1:1 and 1:2 ALD-LZOs in this work.

3.3. Film thickness, crystallinity, morphology, and composition

We further investigated the growth of 1:1 and 1:2 ALD-LZOs on N-GNS. Figure 3a-c shows the SEM images of pristine N-GNS under different magnifications. The thickness of the wrinkles of the N-GNS are typically less than ~3 nm. With the deposition of the 1:1 ALD-LZO, as shown in Figure 3d-f, the thickness of wrinkles of the N-GNS changed to ~24, ~46, and ~73 nm after 100, 200, and 300 ALD cycles, respectively. We then concluded that the growth per cycle (GPC) of the 1:1 ALD-LZO is ~1.1 Å/super-cycle (GPC = (thickness of coated N-GNS - thickness of pristine N-GNS)/(2 × the ALD cycle number)).[39] Figure 3g-i show the thickness evolutions of the N-GNS wrinkles after the deposition of the 1:2 ALD-LZO for 100, 200, and 300 cycles. These SEM images revealed that the wrinkle thickness of N-GNS was increased to ~25, ~53, and ~77 nm, respectively. Consequently, we concluded that the GPC of the 1:2 ALD-LZO is ~1.2 Å/super-cycle. The 1:1 ALD-LZO films were deposited on N-GNS (Figure S6a) and NMC622 powders (Figure S6b) to identify their crystallinity using synchrotron-based XRD. We found no XRD peaks related to the LZO films and therefore concluded that the resultant 1:1 ALD-LZO films are amorphous.

The resultant films of the 1:1 ALD-LZO were also characterized using AFM. According to the 1.1 Å/cycle GPC for the 1:1 ALD-LZO, the thickness of ALD-LZO 1:1 film after 100 and 300 super-cycles would be ~11 and ~33 nm, respectively. The effects of film thickness on the film topography could be clearly observed as shown in Figure 4a and b. The root mean square (RMS) roughness of the 1:1 ALD-LZO film of 100 and 300 cycles is 1.6 and 2.9 nm, respectively. These results verified that the super-ALD processes of LZOs enables high-quality uniform films.

We further determined the composition of the resultant films of the ALD LZOs using XPS. Based on a 100-cycle 1:1 ALD-LZO film deposited on Si wafers, XPS detected Li, Zr, O, Si, C, and F (Figure 5a), where Si and F elements are due to the substrate. According to Table 1, the atomic ratio of Li:Zr is 7.43:1 which is far much larger than the Li:Zr ratio of ~1.4 estimated using QCM data (supposing LiOH and ZrO_2 from the two sub-ALD processes). These XPS results have been confirmed with two different batches of LZO samples. We further applied depth profiling on the deposited 1:1 LZO film to see the composition evolution with depth and did not detect any remarkable differences on the LZO composition. We thought that this inconsistency between the XPS analyses and the Li:Zr ratio estimation based on the QCM data was mainly due to an inaccurate supposition on the surface reactions of the 1:1 ALD-LZO. The sub-ALD LiOH might have changed the surface reactions of the ALD ZrO_2 as supposed in Equations 2A and 2B. The deposited ZrO_x might also have effects on the sub-ALD LiOH. In other words, there must have been strong interactions between the two sub-ALD processes. We need to point out that the adoption of H_2O as the precursor of the oxygen source is unfavorable to rationally deposit LZOs. In this regard, a more insightful study is needed to reveal the exact surface reactions in the future.

The Li1s, Zr3d and O1s spectra were further analyzed using high-resolution XPS, as included in Figure 5b-d. The Zr-O bond and metal oxygen bond (M-O, M = Ni, Mn, Co) could be clearly observed. There has also much Li_2CO_3 on the sample surface, which should be the oxidation product of lithium compounds (e.g., LiOH). It has been reported that the LiOH film could be easily converted to Li_2CO_3 by exposure to CO_2.[27, 40] The XPS analysis was also used to analyze the composition of the 1:2 ALD-LZO, and there also was a poor-Zr composition revealed, i.e., Li:Zr = 7.06:1, as shown in Figure S7a-d and Table S1. Again, a further study is needed to clarify the effects of the water precursor and the exact surface reactions during super-ALD processes of LZOs.

3.4. Electrochemical performance of LZO-coated NMC622 cathodes.

We also studied the effects of the 1:1 ALD-LZO coating on the electrochemical performance of NMC622. Figure 6a shows the initial charge discharge curves of different samples in the voltage window of 3-4.5 V, where ALD-10, -20, -40, and -60 refer to the NMC622 cathodes coated with 10, 20, 40, and 60 cycles of the 1:1 ALD-LZO, respectively. It is easy to observe from Figure 6a that all the bare and LZO-coated samples show typical charge-discharge curves of NMC622 cathode at 0.1 C (1 C = 180 mAh/g). The bare NMC622 electrode has the lowest discharge specific capacity of 184.4 mAh/g while the ALD-10 cell has the highest one, 194.9 mAh/g. As shown in Table S2, the lower irreversible capacity of the 1:1 ALD-LZO coated cathodes is attributed to the suppression of the formation of SEI by the ALD-LZO surface barrier.[41-42] The rate capability of the bare and LZO-coated NMC622 was investigated in the voltage window of 3.0-4.5 V (Figure 6b). At low current densities (0.1 - 1 C), there has no significant differences in discharge specific capacity among the bare and LZO-coated NMC622 electrodes. When the current density was increased to 3 C or higher, encouragingly, the difference in specific capacity was observable and became more and more evident, especially under 5 and 7 C. The ALD-20 cathode shows the best rate performance. The specific discharge capacity of the ALD-20 cathode at 5 and 7 C is 91 and 50 mAh/g versus71 and 32 mAh/g of the bare NMC622 cathode, respectively. Thus, the ALD-20 electrode accounts for an increase of 28% and 56% at 5 and 7 C, respectively. Furthermore, Figure 6c shows the cycling performance tested at 3 C in the voltage window of 3.0 - 4.5 V. After 100 cycles, the bare NMC622 could only sustain 24% of its initial capacity. In comparison, the ALD-20 cathode could sustain 68% of its initial capacity, followed by 42% for the ALD-40, 27% for the ALD-10, and 15% for the ALD-60 cathode. Thus, one is easy to conclude that the 1:1 ALD-LZO could improve the cyclability of NMC622 remarkably with an optimal LZO coating thickness. In this work, the ALD-20 cathode has the best cyclability and rate capability, suggesting an optimal LZO coating thickness of 2.2 nm. The coating thickness and uniformity of the 20-cycle 1:1 LZO over NMC622 powders has been confirmed by STEM-EDS analysis (Figure S8).

We also analyzed the effects of the LZO coatings on the NMC structural stability. As shown in Figure 7(a-d), the discharge curves of the bare and ALD-20 cathodes were comparatively investigated. Compared with the bare NMC622 cathode (Figure 7a), the ALD-20 cathode (Figure 7c) dropped much slower in its capacity with increased cycles. Furthermore, the ALD-LZO coating exhibited an evident role in inhibiting voltage drop of NMC622, which can be clearly observed from the normalized discharge curves in Figure 7b and d. Obviously, the discharge working voltage of the bare NMC622 cathode decreased more quickly than that of the ALD-20 cathode. This should be ascribed to the beneficial effects of the ALD-LZO coating, such as improving mechanical integrity of the coated NMC622 cathode and mitigating interfacial reactions. We particularly used the synchrotron TXM technique to observe the morphological changes of the bare and ALD-20 electrodes after 200 electrochemical cycles, as shown in Figure 8. Compared to the uncycled bare electrode (Figure 8a,b), the cycled bare electrode showed evident cracks after 200 electrochemical cycles (Figure 8c,d). In contract, the ALD-20 electrode showed no identifiable changes (Figure 8e,f) after 200 charge-discharge cycles. That is, the LZO coating improved the mechanical integrity of the NMC622 electrode.

To clarify the beneficial effect of the ALD-LZO coating in improving interfacial properties of NMC622, we studied the lithium insertion/extraction behaviors of NMC622 cathodes with and without LZO coating. To this end, we measured the cyclic voltammetry (CV) curves of the bare NMC622 and two coated cathodes with 20 cycles of the 1:1 ALD-LZO and 1:2 ALD-LZO, respectively, at various scanning speeds (Figure 9a-c). The lithium-ion diffusion coefficient of the NMC622 electrode can be obtained through analyzing the CV curves, and the calculation process is as follows:

$$I_p = k \times n^{3/2} \times A \times D^{1/2} \times \upsilon^{1/2} \times C \qquad (3)$$

where I_P is the peak current of CV curves, $k = 2.69 \times 10^5$ C/(mol.V$^{1/2}$), n is the number of electrons transferred in electrochemical reaction (n = 1 in this work), A is the electrochemical active area (1.095×10^4 cm^2/g), and D is the lithium ion diffusion coefficient, υ is the sweep rate (V/s), C is the lithium ion concentration in the cathode material (1.631×10^{-2} mol/cm^3). As shown in equation (3), the peak current I_P is linear with $\upsilon^{1/2}$, thus the equation (3) can be simplified as:

$$I_p = b \times \upsilon^{1/2} \qquad (4)$$

where the slope of the linear curve of I_p and $\upsilon^{1/2}$ is

$$b = k \times n^{3/2} \times A \times D^{1/2} \times C \qquad (5)$$

To get the lithium ion diffusion coefficient D, we first got a linear line between I_P and $\upsilon^{1/2}$, then calculated its slope b, and then brought all the coefficients into equation (5). Figure 9d shows the linear relationships between charge-discharge peak currents I_P and $\upsilon^{1/2}$ for NMC622 cathodes with and without LZO films, and we get the lithium ion diffusion D for all the cathodes (Table 2). It can be seen from Table 2 that both the 1:1 and 1:2 ALD-LZO films could improve the lithium-ion conductivity of the coated NMC622 cathodes. In particular, the 20-cycle 1:1 ALD-LZO coating improved the insertion/extraction rates of lithium ions of the coated NMC622 cathode by 3.4 and 2.6 times, respectively. This underlies the improved performance of the ALD-20 cathode.

To illustrate the benefits of the 1:1 LZO coating, we compared the performance of NMC622 electrodes coated by 1:1 LZO, ZrO_2, and Al_2O_3. The results of NMC622 by ALD ZrO_2 and Al_2O_3 coatings have been published previously.[16, 43] In all these cases, 20-cycle coatings of 1:1 LZO, ZrO_2, and Al_2O_3 commonly resulted in the best performance of the coated NMC622 electrodes. In the voltage window of 3. 0 – 4.5 V, the 1:1 LZO-coated NMC622 could sustained a capacity of >100 mAh/g after 100 charge-discharge cycles at 3 C (Figure 6c), while the ZrO_2-coated one enabled a capacity of ~80 mAh/g after 50 charge-discharge cycles at 3 C and the Al_2O_3-coated one sustained a capacity of ~80 mAh/g after 45 charge-discharge cycles at 2 C.[16, 43] To facilitate the comparison, these results have been included Figure S9. Obviously, the 1:1 LZO coating performed much better than the ALD ZrO_2 and Al_2O_3 coatings in improving the performance of the coated NMC622 electrode. It clearly indicates that this Li-containing coating is advantageous over Li-free metal oxide coatings of ZrO_2 and Al_2O_3.

In addition to our efforts discussed above, there are many other studies conducted previously on NMC622 electrodes with various ALD coatings, such as Al_2O_3,[44] TiO_2,[17] TiO_x,[45] Li_xTi_yO,[45] a bilayer of AlW_xF_y/AlF_3,[46] nitrogen (N)-doped $AlPO_4$,[47] TiPO,[48] and TiPON.[48] All these studies commonly confirmed that surface modification via ALD is an effective strategy to mitigate the issues of NMC electrodes and thereby improve NMC electrodes' performance, such as sustainable capacity, rate capability, and cycling stability. These coatings are typically very thin, ranging from the sub-nano scale to a few of nanometers. A desirable coating thickness is closely related to the coatings' properties, such as conductivity and mechanical properties. Among various ALD coatings, oxides are the most instigated ones. Recently, there has an increasing interest in Li-containing oxide coatings, as summarized recently by Meng.[15] Compared to binary oxide coatings, ternary or quaternary Li-containing oxide coatings have potentials to enable higher ionic conductivity and thereby facilitate the transport of Li-ions for better performance of NMC electrodes, as confirmed in this study. In this regard, Ahaliabadeh et al also verified that an ALD Li_xTi_yO coating is more favorable than an ALD TiO_x coating to achieve higher performance of NMC622 electrodes.[45] In addition to oxides, metal fluorides and phosphates represent two important classes of ALD coatings. In the case of NMC622, bilayered AlW_xF_y/AlF_3 and N-doped phosphates have been developed and showed beneficial effects.[46-48] These studies have revealed that it is critical to tune coating compositions for desired NMC electrodes, especially for ternary or more complicated compounds (e.g., Li-containing oxides and N-doped phosphates). Apparently, a large variety of ALD coatings have been on the list to modify NMC electrodes. To best design ALD coatings and understand their underlying mechanisms, however, a systematic study is still needed.

4. Conclusions

In summary, we have studied the growth characteristics of ALD-LZO at different deposition temperatures and different sub-cycle ratios. Our study revealed that the growth of the ALD-LZO is subjected to the influence of the hygroscopic nature of the sub-ALD process of LiOH. As a result, it is important to select suitable ALD parameters of deposition temperature and purging time to mitigate the shielding effect of the physiosorbed water. At 225 ^{o}C, we realized the linear growth of 1:1 and 1:2 ALD-LZO but found that it was difficult to grow 2:1 LZO. Furthermore, we confirmed that the 1:1 ALD-LZO film is beneficial to improve the electrochemical performance of NMC622, in terms of sustainable capacity and rate capability. We also revealed that the 1:1 ALD-LZO coating could remarkably improve the insertion and distraction rates of lithium ions of the coated NMC622 cathode for a few times. Thus, this study is helpful for developing lithium-conductive coatings for better electrochemical performance of LIBs

Author contributions

XM conceived and supervised the project. YL drafted the initial manuscript. XM and XX edited and finalized the manuscript. YL and XW collected and analyzed XPS data. XM and YL conduct QCM measurements, electrochemical measurements, and analyses of electron microscopy. HZ conducted XRD measurements. SKG and MZ conducted the measurements of AFM. XX conducted TXM measurements. XX and XW conducted TXM analyses. All authors performed data analyses and manuscript preparation.

Conflicts of interest

There are no conflicts to declare.

Acknowledgements

XM, MZ, and SKG acknowledge the partial support from the Center for Advanced Surface Engineering, under the National Science Foundation Grant (No. OIA-1457888) and the Arkansas EPSCoR Program, ASSET III. XM and YL appreciate the financial research support from the University of Arkansas, Fayetteville, AR, USA. YL appreciates the financial research support from Fundamental Research Funds for the Central Universities, China (No. 2572021BC04) and Northeast Forestry University.

This research used resources of the Advanced Photon Source, a U.S. Department of Energy (DOE) Office of Science User Facility operated for the DOE Office of Science by Argonne National Laboratory under Contract No. DE-AC02-06CH11357. This research used resources of the beamline FXI/18ID of the National Synchrotron Light Source II, a U.S. Department of Energy (DOE) Office of Science User Facility operated for the DOE Office of Science by Brookhaven National Laboratory under Contract No. DE-SC0012704.

References:

1. Xu, K.; von Cresce, A., Interfacing electrolytes with electrodes in Li ion batteries. *J. Mater. Chem.* **2011,** *21* (27), 9849-9864.

2. Palacín, M. R.; de Guibert, A., Why do batteries fail? *Science* **2016,** *351* (6273).

3. Winter, M., The solid electrolyte interphase -- the most important and the least understood solid electrolyte in rechargeable Li batteries. *Z. Phys. Chem.* **2009,** *223* (10-11), 1395-1406.

4. Myung, S.-T.; Amine, K.; Sun, Y.-K., Surface modification of cathode materials from nano- to microscale for rechargeable lithium-ion batteries. *J. Mater. Chem.* **2010,** *20* (34), 7074-7095.

5. Fu, L. J.; Liu, H.; Li, C.; Wu, Y. P.; Rahm, E.; Holze, R.; Wu, H. Q., Surface modifications of electrode materials for lithium ion batteries. *Solid State Sci.* **2006,** *8* (2), 113-128.

6. Li, T.; Yuan, X.-Z.; Zhang, L.; Song, D.; Shi, K.; Bock, C., Degradation mechanisms and mitigation strategies of nickel-rich NMC-based lithium-ion batteries. *Electrochemical Energy Reviews* **2020,** *3* (1), 43-80.

7. Guan, P.; Zhou, L.; Yu, Z.; Sun, Y.; Liu, Y.; Wu, F.; Jiang, Y.; Chu, D., Recent progress of surface coating on cathode materials for high-performance lithium-ion batteries. *Journal of Energy Chemistry* **2020,** *43*, 220-235.

8. Meng, X.; Yang, X. Q.; Sun, X. L., Emerging applications of atomic layer deposition for lithium-ion battery studies. *Adv. Mater.* **2012,** *24* (27), 3589-3615.

9. Meng, X., Atomic and molecular layer deposition in pursuing better batteries. *J. Mater. Res.* **2021,** *36*, 2-25.

10. George, S. M., Atomic layer deposition: an overview. *Chem. Rev.* **2010,** *110* (1), 111-131.

11. Elam, J. W.; Dasgupta, N. P.; Prinz, F. B., ALD for clean energy conversion, utilization, and storage. *MRS bulletin* **2011,** *36* (11), 899-906.

12. Liu, Y.; Wang, X.; Cai, J.; Han, X.; Geng, D.; Li, J.; Meng, X., Atomic-scale tuned interface of nickel-rich cathode for enhanced electrochemical performance in lithium-ion batteries. *J Mater Sci Technol* **2020**.

13. Bloom, I.; Trahey, L.; Abouimrane, A.; Belharouak, I.; Zhang, X. F.; Wu, Q. L.; Lu, W. Q.; Abraham, D. P.; Bettge, M.; Elam, J. W.; Meng, X. B.; Burrell, A. K.; Ban, C. M.; Tenent, R.; Nanda, J.; Dudney, N., Effect of interface modifications on voltage fade in $0.5Li_2MnO_3.0.5LiNi_{0.375}Mn_{0.375}CO_{0.25}O_2$ cathode materials. *J. Power Sources* **2014,** *249*, 509-514.

14. Park, J. S.; Meng, X. B.; Elam, J. W.; Hao, S. Q.; Wolverton, C.; Kim, C.; Cabana, J., Ultrathin lithium-ion conducting coatings for increased interfacial stability in high voltage lithium-ion batteries. *Chem. Mater.* **2014,** *26* (10), 3128-3134.

15. Meng, X., Atomic layer deposition of solid-state electrolytes for next-generation lithium-ion batteries and beyond: Opportunities and challenges. *Energy Storage Materials* **2020,** *30*, 296-328.

16. Wang, X.; Cai, J.; Liu, Y.; Han, X.; Ren, Y.; Li, J.; Liu, Y.; Meng, X., Atomic-scale constituting stable interface for improved $LiNi_{0.6}Mn_{0.2}Co_{0.2}O_2$ cathodes of lithium-ion batteries. *Nanotechnology* **2021,** *32* (11), 115401.

17. Gao, H.; Cai, J.; Xu, G.-L.; Li, L.; Ren, Y.; Meng, X.; Amine, K.; Chen, Z., Surface Modification for Suppressing Interfacial Parasitic Reactions of a Nickel-Rich Lithium-Ion Cathode. *Chemistry of Materials* **2019,** *31* (8), 2723-2730.

18. Kim, J.; Lee, H.; Cha, H.; Yoon, M.; Park, M.; Cho, J., Prospect and reality of Ni-rich cathode for commercialization. *Adv. Energy Mater.* **2018,** *8* (6), 1702028.

19. Manthiram, A.; Song, B.; Li, W., A perspective on nickel-rich layered oxide cathodes for lithium-ion batteries. *Energy Storage Materials* **2017,** *6*, 125-139.

20. Zhang, S. S., Understanding of performance degradation of LiNi0.80Co0.10Mn0.10O2 cathode material operating at high potentials. *Journal of Energy Chemistry* **2020,** *41*, 135-141.

21. Zhang, S. S., Problems and their origins of Ni-rich layered oxide cathode materials. *Energy Storage Materials* **2020,** *24*, 247-254.

22. Li, X.; Liu, J.; Banis, M. N.; Lushington, A.; Li, R.; Cai, M.; Sun, X., Atomic layer deposition of solid-state electrolyte coated cathode materials with superior high-voltage cycling behavior for lithium ion battery application. *Energy Environ. Sci.* **2014,** *7* (2), 768-778.

23. Xie, J.; Sendek, A. D.; Cubuk, E. D.; Zhang, X.; Lu, Z.; Gong, Y.; Wu, T.; Shi, F.; Liu, W.; Reed, E. J.; Cui, Y., Atomic layer deposition of stable $LiAlF_4$ lithium ion conductive interfacial layer for stable cathode cycling. *ACS Nano* **2017,** *11*, 7019-7027.

24. Yan, P.; Zheng, J.; Liu, J.; Wang, B.; Cheng, X.; Zhang, Y.; Sun, X.; Wang, C.; Zhang, J.-G., Tailoring grain boundary structures and chemistry of Ni-rich layered cathodes for enhanced cycle stability of lithium-ion batteries. *Nature Energy* **2018,** *3* (7), 600-605.

25. Lin, C.-F.; Fan, X.; Pearse, A.; Liou, S.-C.; Gregorczyk, K.; Leskes, M.; Wang, C.; Lee, S. B.; Rubloff, G. W.; Noked, M., Highly Reversible Conversion-Type FeOF Composite Electrode with Extended Lithium Insertion by Atomic Layer Deposition LiPON Protection. *Chem. Mater.* **2017,** *29* (20), 8780-8791.

26. Kozen, A. C.; Pearse, A. J.; Lin, C.-F.; Noked, M.; Rubloff, G. W., Atomic layer deposition of the solid electrolyte LiPON. *Chem. Mater.* **2015,** *27* (15), 5324-5331.

27. Cavanagh, A. S.; Lee, Y.; Yoon, B.; George, S. M., Atomic layer deposition of LiOH and Li_2CO_3 using lithium t-butoxide as the lithium source. *Atomic Layer Deposition Applications 6* **2010,** *33* (2), 223-229.

28. Comstock, D. J.; Elam, J. W., Mechanistic study of lithium aluminum oxide atomic layer deposition. *J. Phys. Chem. C* **2013,** *117* (4), 1677-1683.

29. Liu, J.; Banis, M. N.; Li, X. F.; Lushington, A.; Cai, M.; Li, R. Y.; Sham, T. K.; Sun, X. L., Atomic layer deposition of lithium tantalate solid-state electrolytes. *J. Phys. Chem. C* **2013,** *117* (39), 20260-20267.

30. Wang, B.; Zhao, Y.; Banis, M. N.; Sun, Q.; Adair, K. R.; Li, R.; Sham, T.-K.; Sun, X., Atomic layer deposition of lithium niobium oxides as potential solid-state electrolytes for lithium-ion batteries. *ACS Appl. Mater. Interfaces* **2018,** *10* (2), 1654-1661.

31. Wang, X.; Ghosh, S. K.; Afshar-Mohajer, M.; Zhou, H.; Liu, Y.; Han, X.; Cai, J.; Zou, M.; Meng, X., Atomic layer deposition of zirconium oxide thin films. *J. Mater. Res.* **2019,** *35* (7), 804-812.

32. Liu, J.; Meng, X. B.; Banis, M. N.; Cai, M.; Li, R. Y.; Sun, X. L., Crystallinity-controlled synthesis of zirconium oxide thin films on nitrogen-doped carbon nanotubes by atomic layer deposition. *J. Phys. Chem. C* **2012,** *116* (27), 14656-14664.

33. Liu, J.; Meng, X.; Hu, Y.; Geng, D.; Banis, M. N.; Cai, M.; Li, R.; Sun, X., Controlled synthesis of zirconium oxide on graphene nanosheets by atomic layer deposition and its growth mechanism. *Carbon* **2013,** *52*, 74-82.

34. Cavanagh, A. S.; Lee, Y.; Yoon, B.; George, S., Atomic layer deposition of LiOH and Li2CO3 using lithium t-butoxide as the lithium source. *ECS transactions* **2010,** *33* (2), 223-229.

35. Meng, X.; Libera, J. A.; Fister, T. T.; Zhou, H.; Hedlund, J. K.; Fenter, P.; Elam, J. W., Atomic layer deposition of gallium sulfide films using hexakis(dimethylamido)digallium and hydrogen sulfide. *Chem. Mater.* **2014,** *26* (2), 1029-1039.

36. Meng, X.; Cao, Y.; Libera, J. A.; Elam, J. W., Atomic layer deposition of aluminum sulfide: Growth mechanism and electrochemical evaluation in lithium-ion batteries. *Chem. Mater.* **2017,** *29* (21), 9043-9052.

37. Meng, X.; Comstock, D. J.; Fister, T. T.; Elam, J. W., Vapor-phase atomic-controllable growth of amorphous Li_2S for high-performance lithium–sulfur batteries. *ACS Nano* **2014,** *8* (10), 10963-10972.

38. Comstock, D. J.; Elam, J. W., Mechanistic Study of Lithium Aluminum Oxide Atomic Layer Deposition. *J. Phys. Chem. C* **2013,** *117* (4), 1677-1683.

39. Meng, X.; Geng, D.; Liu, J.; Li, R.; Sun, X., Controllable synthesis of graphene-based titanium dioxide nanocomposites by atomic layer deposition. *Nanotechnology* **2011,** *22* (16), 165602.

40. Smyrl, N.; Fuller Jr, E.; Powell, G., Monitoring the heterogeneous reaction of LiH and LiOH with H2O and CO2 by diffuse reflectance infrared fourier transform spectroscopy. *Applied Spectroscopy* **1983,** *37* (1), 38-44.

41. Tang, Y.; Han, X.; Zhang, W.; He, Y., La doping and coating enabled by one-step method for high performance Li1.2Mn0.54Ni0.13Co0.13O2 Li-rich cathode. *Ionics*

(Kiel) **2020,** *26* (8), 3737-3747.

42. Qian, R.; Liu, Y.; Cheng, T.; Li, P.; Chen, R.; Lyu, Y.; Guo, B., Enhanced Surface Chemical and Structural Stability of Ni-Rich Cathode Materials by Synchronous Lithium-Ion Conductor Coating for Lithium-Ion Batteries. *ACS Appl Mater Interfaces* **2020**.

43. Liu, Y.; Wang, X.; Cai, J.; Han, X.; Geng, D.; Li, J.; Meng, X., Atomic-scale tuned interface of nickel-rich cathode for enhanced electrochemical performance in lithium-ion batteries. *Journal of Materials Science & Technology* **2020,** *54*, 77-86.

44. Neudeck, S.; Mazilkin, A.; Reitz, C.; Hartmann, P.; Janek, J.; Brezesinski, T., Effect of Low-Temperature Al2O3 ALD Coating on Ni-Rich Layered Oxide Composite Cathode on the Long-Term Cycling Performance of Lithium-Ion Batteries. *Sci. Rep.* **2019,** *9* (1), 5328.

45. Ahaliabadeh, Z.; Miikkulainen, V.; Mäntymäki, M.; Mousavihashemi, S.; Lahtinen, J.; Lide, Y.; Jiang, H.; Mizohata, K.; Kankaanpää, T.; Kallio, T., Understanding the Stabilizing Effects of Nanoscale Metal Oxide and Li–Metal Oxide Coatings on Lithium-Ion Battery Positive Electrode Materials. *ACS Appl. Mater. Interfaces* **2021,** *13* (36), 42773-42790.

46. Gutierrez, A.; Choudhury, D.; Sharifi-Asl, S.; Yonemoto, B. T.; Shahbazian-Yassar, R.; Mane, A. U.; Elam, J. W.; Croy, J., Multifunctional Films Deposited by Atomic Layer Deposition for Tailored Interfaces of Electrochemical Systems. *J. Electrochem. Soc.* **2020,** *167* (14), 140541.

47. Henderick, L.; Hamed, H.; Mattelaer, F.; Minjauw, M.; Meersschaut, J.; Dendooven, J.; Safari, M.; Vereecken, P.; Detavernier, C., Atomic Layer Deposition of Nitrogen-Doped Al Phosphate Coatings for Li-Ion Battery Applications. *ACS Appl. Mater. Interfaces* **2020,** *12* (23), 25949-25960.

48. Henderick, L.; Hamed, H.; Mattelaer, F.; Minjauw, M.; Nisula, M.; Meersschaut, J.; Dendooven, J.; Safari, M.; Vereecken, P.; Detavernier, C., Plasma enhanced atomic layer deposition of a (nitrogen doped) Ti phosphate coating for improved energy storage in Li-ion batteries. *J. Power Sources* **2021,** *497*, 229866.

Table Captions

Table 1. Element composition and quantitative analysis of 1:1 ALD-LZO

Table 2 Lithium-ion diffusion coefficients of bare NMC622 and NMC622 cathodes coated with 20 cycles 1:1 LZO and 1:2 LZO.

Table 1

Elements	***Peak BE***	***FWHM eV***	***Atomic %***
Li 1s	55.50	2.10	13.15
Zr 3d	183.45	4.57	1.77
O 1s	531.83	3.52	35.57
Si 2p	100.04	3.12	29.70
C 1s	285.09	3.04	17.44
F 1s	685.12	2.83	2.36

Table 2

Samples	$D_{Li\text{-}insertion}$（cm^2/s）	$D_{Li\text{-}extraction}$（cm^2/s）
Bare	5.60×10^{-12}	8.16×10^{-12}
1:1 ALD-LZO	1.91×10^{-11}	2.14×10^{-11}
1:2 ALD-LZO	7.38×10^{-12}	9.11×10^{-12}

Figure Captions:

Figure 1. *In-situ* QCM measurements of ALD-LZOs using the timing sequence of LTB (3 s) – purge (60 s) - H_2O (0.015 s) – purge (60 s) - TDMA-Zr (0.03 s) – purge (60 s) - H_2O (0.015 s) – purge (60 s) at 175 (a, b and c), 200 (d, e and f) and 225 °C (g and h). (i) Comparison of the *in-situ* QCM data of 1:1 LZO for 50 consecutive ALD cycles at these three temperatures. (a), (d) and (g) show 50 consecutive cycles, (b) and (e) are enlarged views of 3 consecutive cycles in Region I, (c) and (f) are enlarged views of three consecutive cycles in Region II, and (h) is an enlarged view of three cycles in (g). The right axis in (b), (c), (e), (f), and (h) is for precursor vapor pressure.

Figure 2. In-situ QCM measurements of 1:2 ALD-LZO using the timing sequence of LiO^tBu (3 s) – purge (60 s) - H_2O (0.03 s) – purge (60 s) - TDMA-Zr (0.03 s) – purge (60 s) - H_2O (0.015 s) – purge (60 s) - TDMA-Zr (0.03 s) – purge (60 s) - H_2O (0.015 s) – purge 60 s at 225 °C: (a) 50 consecutive cycles and (b) an enlarged view of 3 cycles.

Figure 3. SEM images of pristine N-GNS (a, b, c) and N-GNS coated with different number of cycles of the 1:1 ALD-LZO (d, e, f) and 1:2 ALD-LZO (g, h, i) films. (d) and (g) are the N-GNS coated for 100 cycles, (e) and (h) are the N-GNS coated for 200 cycles, and (f) and (i) are the N-GNS coated for 300 cycles.

Figure 4. AFM images of 1:1 ALD-LZO films deposited on Si wafer for (a) 100 and (b) 300 super-cycles at 225 °C. The RMS roughness values are 1.6 and 2.9 nm, respectively.

Figure 5. (a) The XPS survey of the 1:1 ALD-LZO film. (b), (c) and (d) are high-precision XPS spectra of Li1s, Zr3d and O1s, respectively.

Figure 6. (a) The first cycle of charge and discharge curves of the bare NMC622 and NMC622 coated with 1:1 ALD-LZO for different cycles at 3.0-4.5 V and 0.1 C (1 C = 180 mAh/g), (b) Rate performance of different NMC622 samples at 3.0-4.5 V, (c) Cycling performance of different NMC622 samples at 3.0-4.5 V and 3 C (1 C = 180 mAh/g).

Figure 7. Charge-discharge curves of bare (a, b) and ALD-20 samples (c, d) at 3.0-4.5 V and 3 C, where (a, c) is the measured specific capacity voltage curves and (b, d) is the normalized specific capacity voltage curves.

Figure 8. TXM images of (a, b, c, d) the bare and (e, f) the ALD-20 NMC622 cathodes. (a, b) the bare NMC622 electrode before electrochemical cycles and (c, d, e, f) the electrodes after 200 electrochemical cycles in the voltage window of 3.0-4.5 V at 3 C (1 C = 180 mAh/g). (b, d, f) are the corresponding enlarged images of the blue box in (a, c, e).

Figure 9. Cyclic voltammetry curves (CV) at various scanning rates (0.1, 0.2, 0.3, 0.4, 0.5, 0.6, 0.7, 0.8, 0.9, and 1.0 mV/s) between 3.0-4.5 V. (a) Bare NMC622, (b) NMC622 cathodes coated with 20 cycles 1:1 LZO, (c) NMC622 cathode coated with 20 cycles 1:2 LZO. (d) Linear curve relationship between maximum peak current of charge and discharge and square root of sweep speed.

Figures:

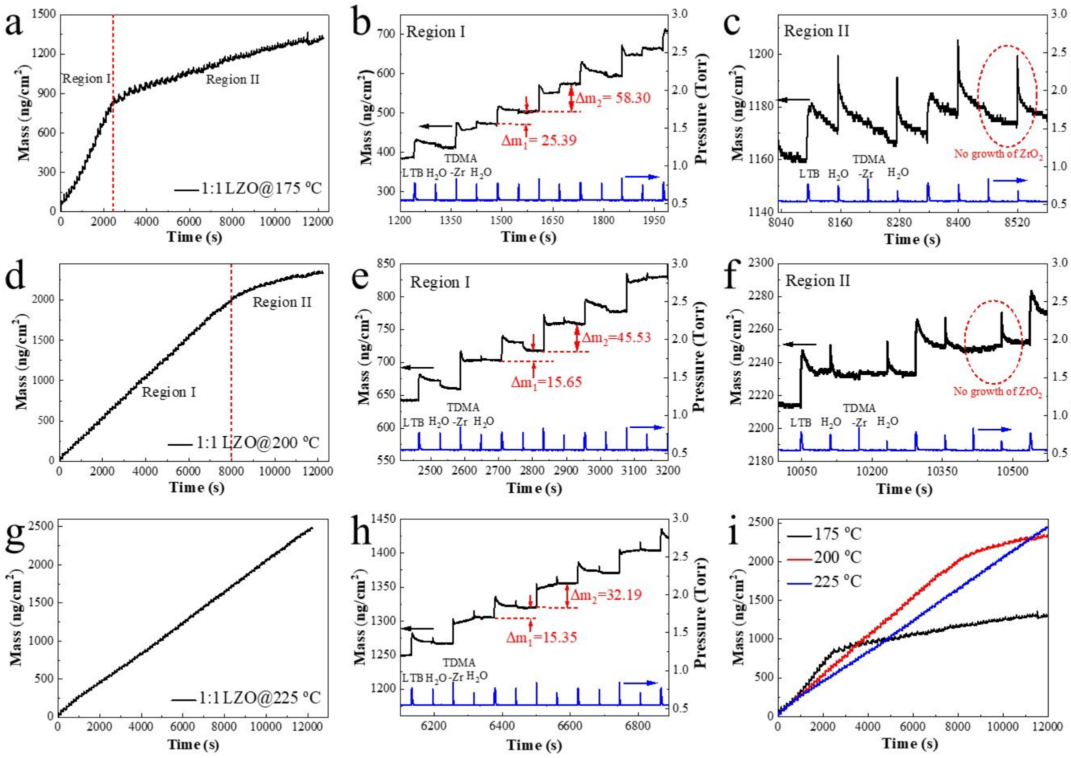

Figure 1

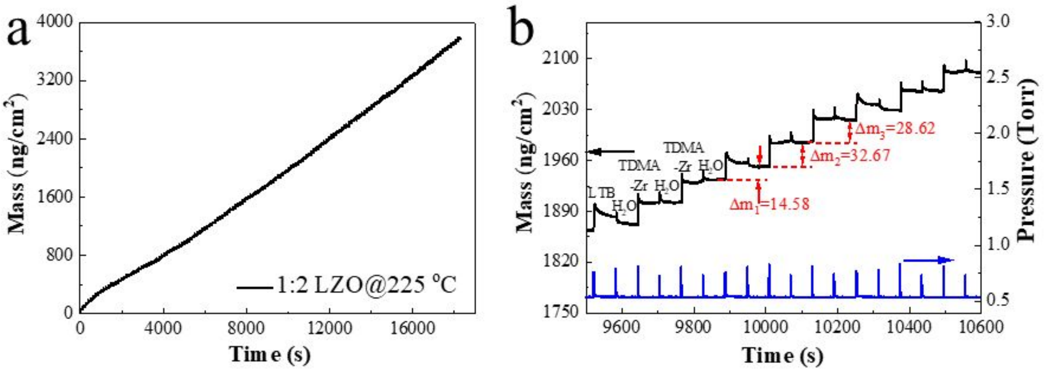

Figure 2

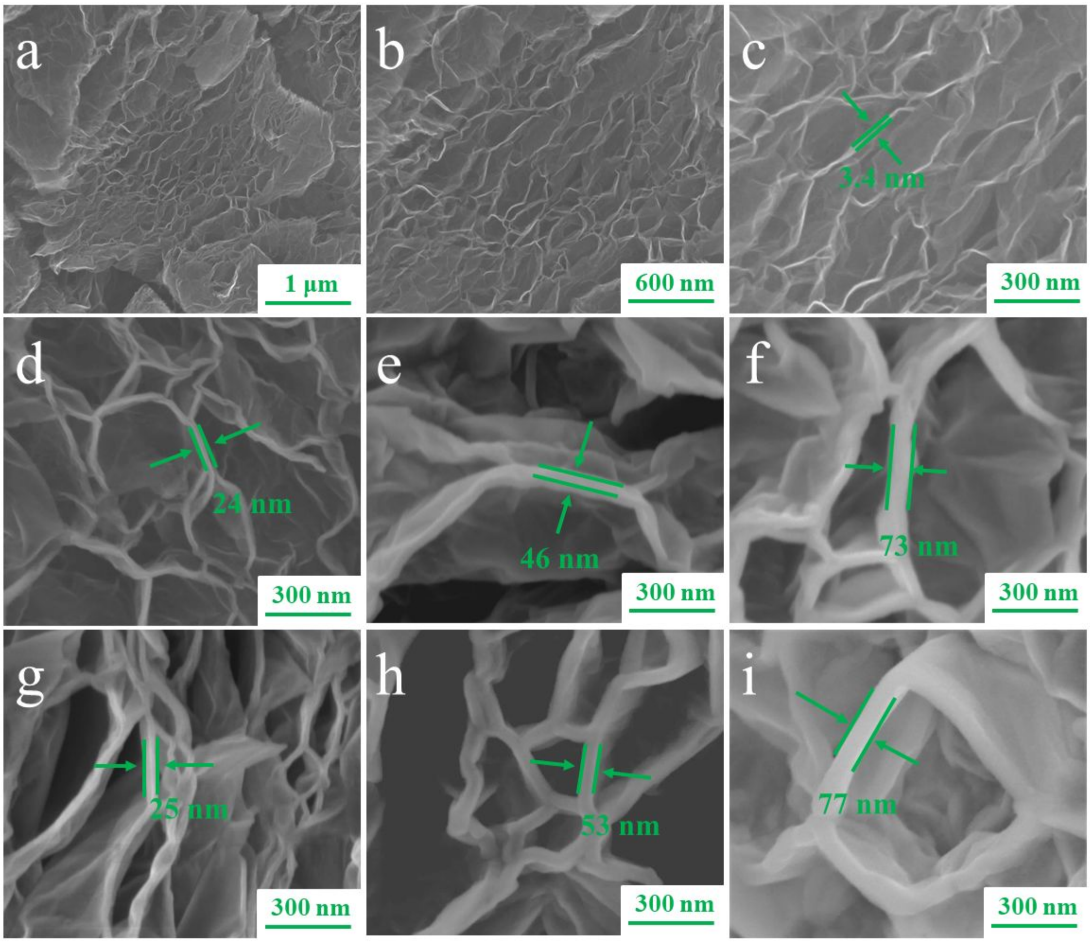

Figure 3

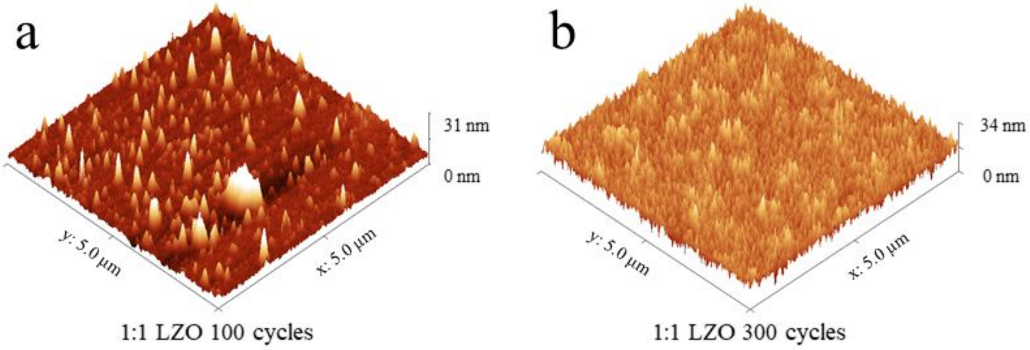

1:1 LZO 100 cycles

1:1 LZO 300 cycles

Figure 4

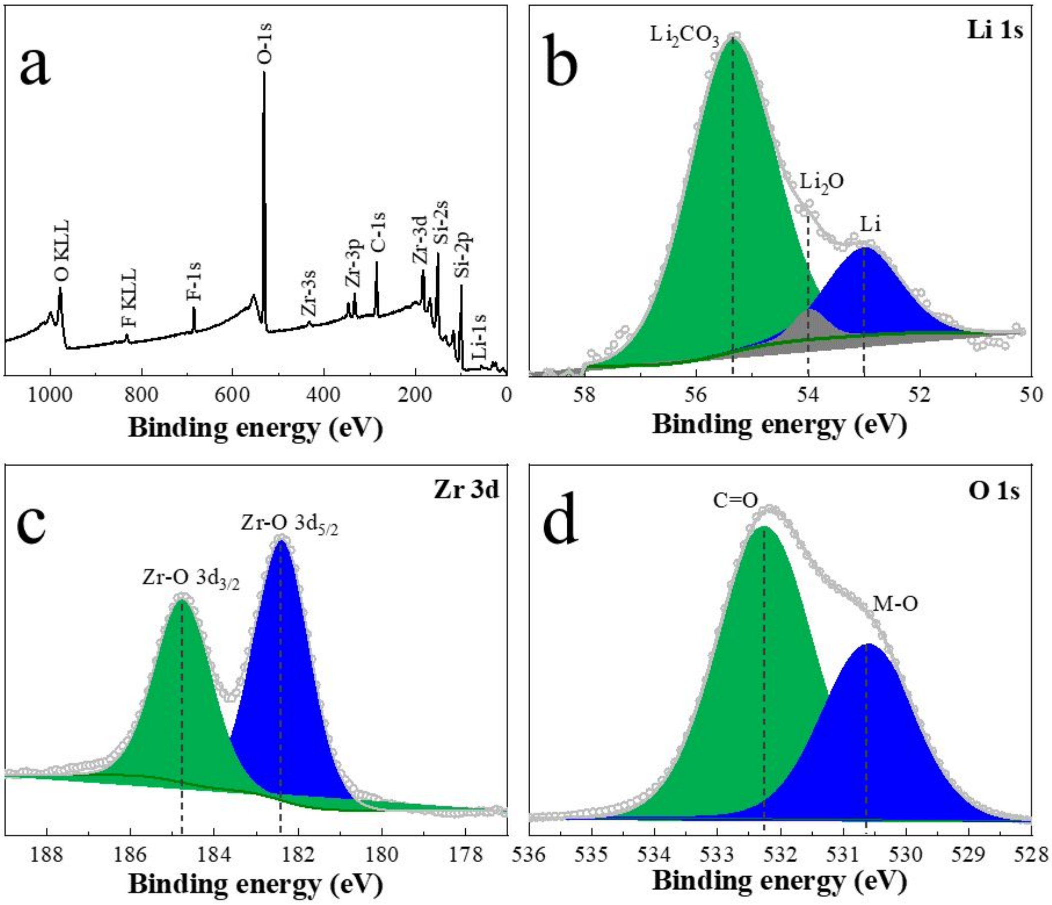
a
O KLL
F KLL
F-1s
O-1s
Zr-3s
Zr-3p
C-1s
Zr-3d
Si-2s
Si-2p
Li-1s
1000
800
600
400
200
0
Binding energy (eV)
b
Li 1s
Li_2CO_3
Li_2O
Li
58
56
54
52
50
Binding energy (eV)
c
Zr 3d
Zr-O $3d_{5/2}$
Zr-O $3d_{3/2}$
188
186
184
182
180
178
Binding energy (eV)
d
O 1s
C=O
M-O
536
535
534
533
532
531
530
529
528
Binding energy (eV)

Figure 5

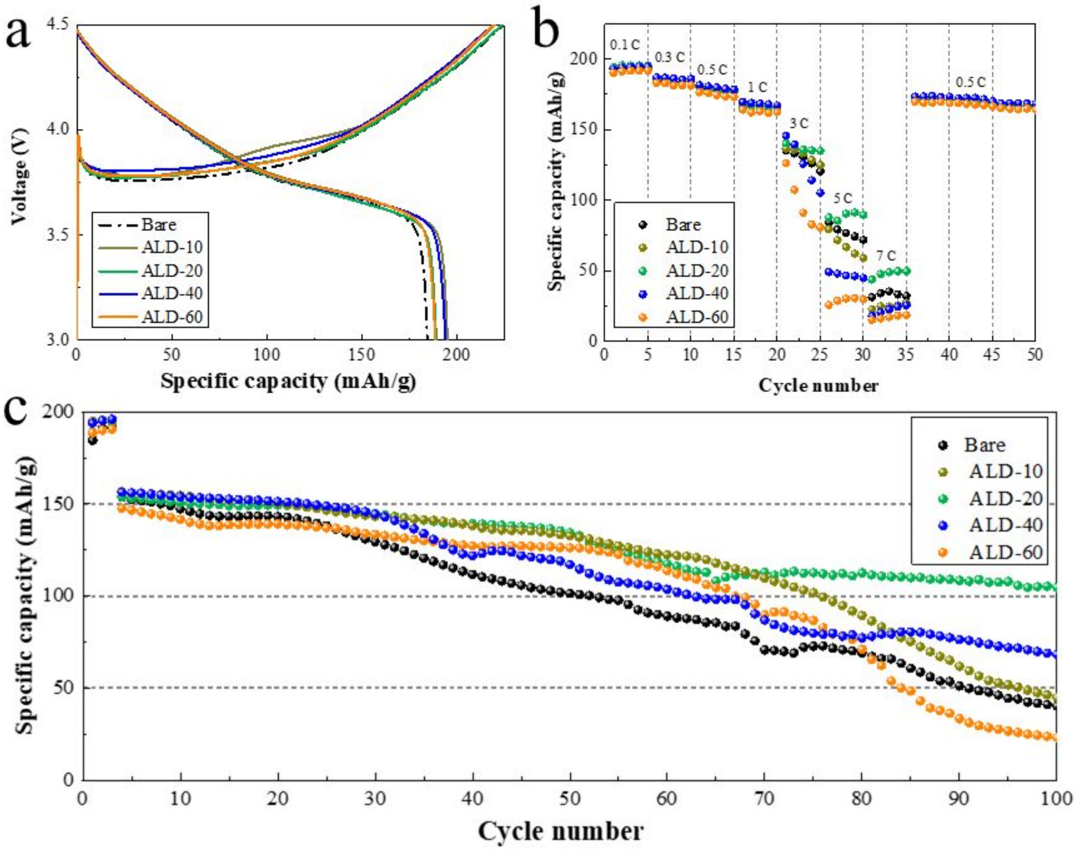
a
Voltage (V)
Specific capacity (mAh/g)
4.5
4.0
3.5
3.0
0
50
100
150
200
Bare
ALD-10
ALD-20
ALD-40
ALD-60
b
Specific capacity (mAh/g)
Cycle number
0.1 C
0.3 C
0.5 C
1 C
3 C
5 C
7 C
0.5 C
200
150
100
50
0
0
5
10
15
20
25
30
35
40
45
50
Bare
ALD-10
ALD-20
ALD-40
ALD-60
c
Specific capacity (mAh/g)
Cycle number
200
150
100
50
0
0
10
20
30
40
50
60
70
80
90
100
Bare
ALD-10
ALD-20
ALD-40
ALD-60

Figure 6

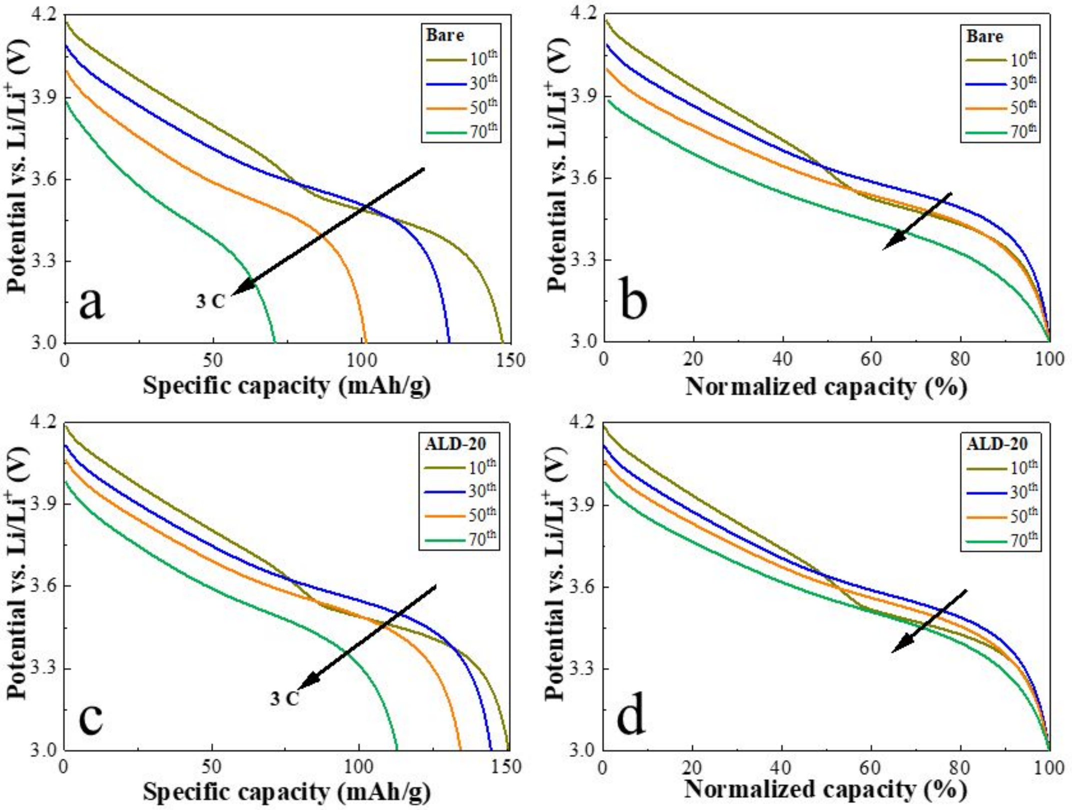
a
b
c
d
Bare
ALD-20
10th
30th
50th
70th
3 C
Potential vs. Li/Li+ (V)
Specific capacity (mAh/g)
Normalized capacity (%)
4.2
3.9
3.6
3.3
3.0
0
50
100
150
20
40
60
80

Figure 7

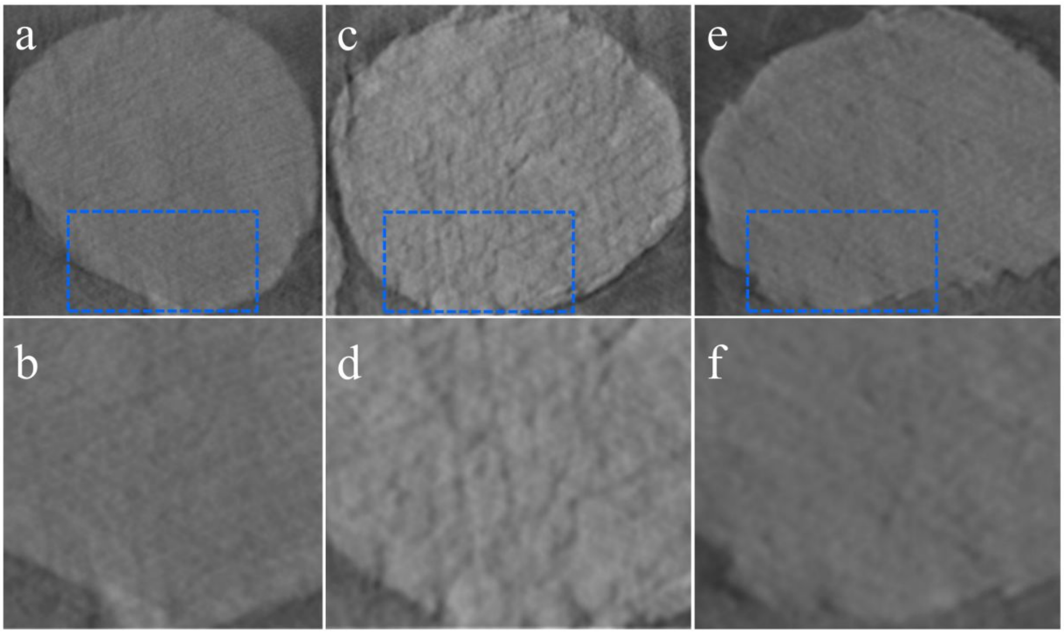

Figure 8

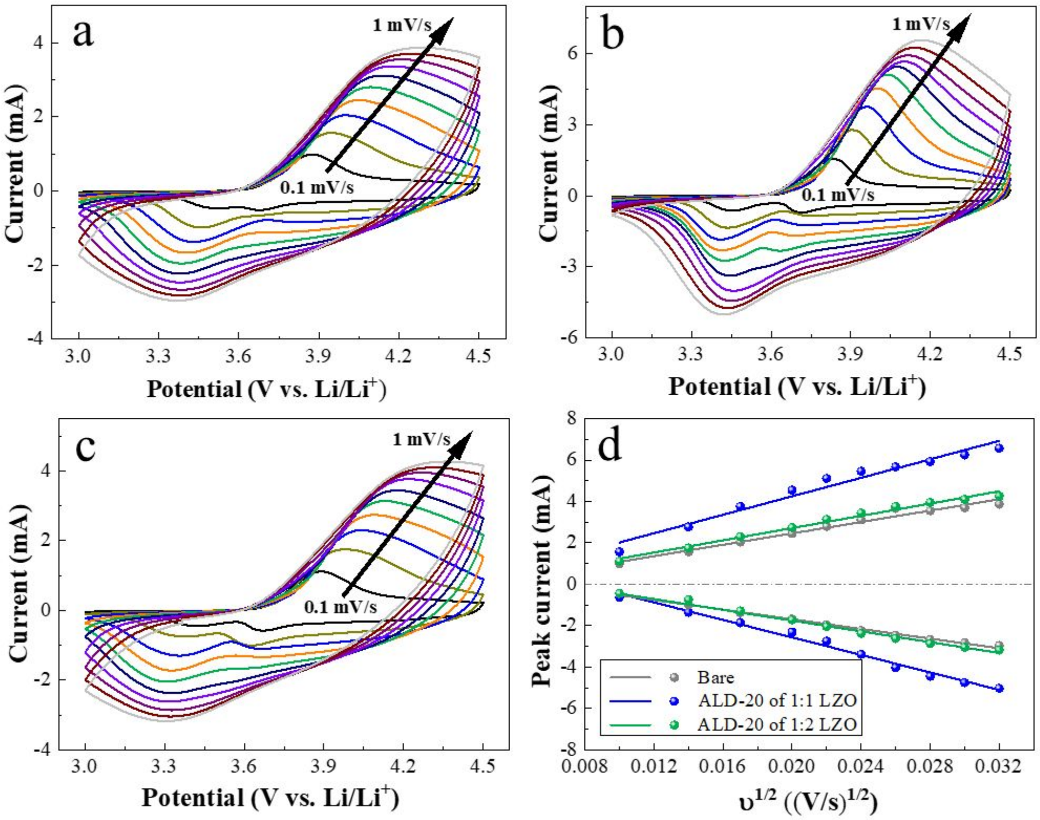

Figure 9